

Evolution of Intermediate Water Masses Based on Argo Float Displacements

F. SÉVELLEC

Ocean and Earth Science, University of Southampton, Southampton, United Kingdom

A. COLIN DE VERDIÈRE AND M. OLLITRAULT

Laboratoire d'Océanographie Physique et Spatiale (UMR 6523 CNRS IFREMER IRD UBO), Brest, France

(Manuscript received 30 August 2016, in final form 1 March 2017)

ABSTRACT

The evolution and dispersion of intermediate water masses in the ocean interior is studied. To this purpose, an empirical statistical model of Lagrangian tracers at a constant depth level is developed. The model follows the transfer operator based on 10-day deep displacements of Argo floats at ~ 1000 m depth. An asymptotic analysis of the model shows the existence of 10 principal stationary points (the 10 locations attract asymptotically 97% of the tracers). It takes ~ 1000 years to reach this asymptotic regime relevant for estimating the stationary points. For Lagrangian floats, the concept of attractor needs to be generalized in a statistical sense (versus deterministic), except for a few places in the ocean. In this new framework, a tracer has a likelihood to reach the stationary points, rather than a certainty to reach a single stationary point. The empirical statistical model is used to describe the fate of three intermediate water masses: North Pacific Intermediate Water (NPIW), Mediterranean Water (MW), and Antarctic Intermediate Water (AAIW). These experiments show a dramatic difference in the long-time behavior of NPIW, MW, and AAIW. In the permanent regime, the NPIW concentrates locally (in the Kuroshio recirculation) and the MW remains mainly regional (concentrated in the subtropical gyre of the North Atlantic), whereas the AAIW spreads globally (well mixed throughout the entire ocean).


1. Introduction

Water mass can be defined as a consistent and continuous volume of ocean water with fairly constant properties in terms of temperature and salinity, and can thus be easily identified through a classical θ - S diagram. Water masses set their θ - S properties at the ocean surface when in contact with the atmosphere. These properties are then conserved during their subsurface journey, to the limit of weak mixing between neighboring water masses. It is thus quite natural to track water masses from observations using their θ - S properties.

Because of their subsurface journey, water masses are at the core of mass, heat, and freshwater transports and redistribution, both at local and global scales (Gordon

1986; Talley 1999, 2003). Hence, this ocean decomposition in water masses provides a thermodynamical alternative to the more classical dynamical paradigm to understand the global ocean circulation (e.g., Zika et al. 2010, 2012).

One particular subcategory of water masses is the intermediate water masses that can be loosely placed between 500 and 1500 m, that is, below the upper ocean characterized by the mode waters and above the deep ocean characterized by the deep waters. These water masses have the property of corresponding to either a salinity minimum or maximum in the vertical. It is through this property that they are tracked in the ocean. Note that at the interface between two water masses, the mixing might blur the exact separation and complicate the use of this diagnostic. Because of their high or low salinity value, they are crucial in setting up the ocean freshwater transport. Hence, determining their subsurface journey is fundamental for a better understanding of the global ocean

 Denotes content that is immediately available upon publication as open access.

Corresponding author: F. Sévellec, florian.sevellec@noc.soton.ac.uk



This article is licensed under a Creative Commons Attribution 4.0 license (<http://creativecommons.org/licenses/by/4.0/>).

circulation, and in particular the meridional overturning circulation (Srokosz et al. 2012) and its stability, which has been demonstrated to be sensitive to the freshwater transport (e.g., Weaver et al. 1991; Cimadoribus et al. 2012; Sévellec and Fedorov 2014).

Recent progresses in monitoring the global ocean have been tightly linked to the development of the Argo program over the last two decades. Argo is an operational global array of more than 3000 independent profiling floats that periodically measures temperature and salinity from 2000 m to the surface. A majority of floats drift near 1000 m for near 10-day periods between their return trips to the surface, during which they record temperature and salinity. These drifts are particularly interesting for the study of water masses. Indeed, beyond classical hydrography, an alternative way to track water masses is through the use of Lagrangian floats, as often done in numerical model studies (e.g., Rimaud et al. 2012). The ~ 1000 m depth of Argo floats allows the study of three intermediate water masses: North Pacific Intermediate Water (NPIW), Mediterranean Water (MW), and Antarctic Intermediate Water (AAIW).

In this study we will take advantage of these Argo deep displacements to estimate the spreading of intermediate water masses. This will be done by transforming the individual deterministic displacement of each float into a global probabilistic function valid for all floats. This is achieved by determining the transfer operator of float displacement. This method is widely used in statistical physics (e.g., Lucarini 2016) and has been shown to be useful to interpret geophysical behavior, such as atmospheric blocking events (Tantet et al. 2015) or detection of oceanic eddies (Froyland et al. 2007), for instance. This classical tool of dynamical system theory is often applied to study the evolution of a system by gathering information from its trajectory in the phase space, rather than the trajectory in the physical space as here, but the principle remains identical. This method has the advantage of transforming a complex system into a tractable linear one. However, the deterministic information on the behavior of a single trajectory is lost and only the probabilistic information on the evolution of the density of trajectories is retained. In this sense, it is well suited for tracking statistical properties determined by a large number of trajectories, such as water masses, rather than evolution of single trajectory.

When the idea of massive floats deployments was being discussed during the World Ocean Circulation Experiment (WOCE) planning sessions, F. Bretherton (1985, personal communication) envisioned the use of transition probabilities for reconstructing the joint large-scale distributions of the mean circulation and turbulent diffusion using numerical floats computed from ocean models.

Thirty years later, it becomes possible to construct such transition probabilities with real float data.

In this study, we determine the transfer operator of float density near the 1000-m-depth surface based on 10-day deep displacements of individual Argo floats. This model of tracer displacements determines asymptotically the possible attractors of the floats and their corresponding basins of attraction. After the model development and first analysis, the transfer operator is used to track intermediate water masses (more specifically, NPIW, MW, and AAIW). It is important to note that our alternative method, through the use of the transfer operator, overcomes the difficulty of tracking water masses up to their edges, as discussed for the classical method. Indeed, the probabilistic approach will determine everywhere the exact proportion of water coming from a particular water mass source, although, in some locations, the tracked water mass may not be dominant. Also, unlike the classical method, it gives us the entire evolution of water masses, which is particularly useful to determine adjustment time scales.

In section 2, the empirical statistical model, based on the transfer operator, will be developed. In section 3, results from asymptotic analyses of the model will be given. Application of the model to the spread of intermediate water masses is presented in section 4, and conclusions are drawn in section 5.

2. Statistical Lagrangian model

a. Method

In this section we describe the statistical model for the time evolution of Argo float distribution near ~ 1000 m depth. To this purpose, we split Earth's surface into $4^\circ \times 4^\circ$ square boxes (Fig. 1) to achieve a good balance between high spatial resolution and high numbers of floats. To evaluate the Lagrangian displacement statistics, we count the number of Lagrangian floats in each box before their sinking $N(i, j)$ (where $i \in [1, 90]$ and $j \in [1, 45]$ are the box indices for longitude and latitude, respectively) and after one cycle underwater journey $n(i, j)$. Examples of the number of floats found before sinking in four individual grid cells and their distribution after surfacing 10 days later are given in Fig. 2, using the ANDRO dataset described in the next section.

A transfer matrix associated to a particular initial (i_0, j_0) box can then be defined as follows:

- This is a square matrix with 90×45 (thus 4050) rows and 4050 columns (covering the entire globe including land).
- The column index $i_0 + (j_0 - 1) \times 90$ corresponds to the initial (i_0, j_0) box, the row indices correspond to the final boxes, and the matrix elements are the ratios of

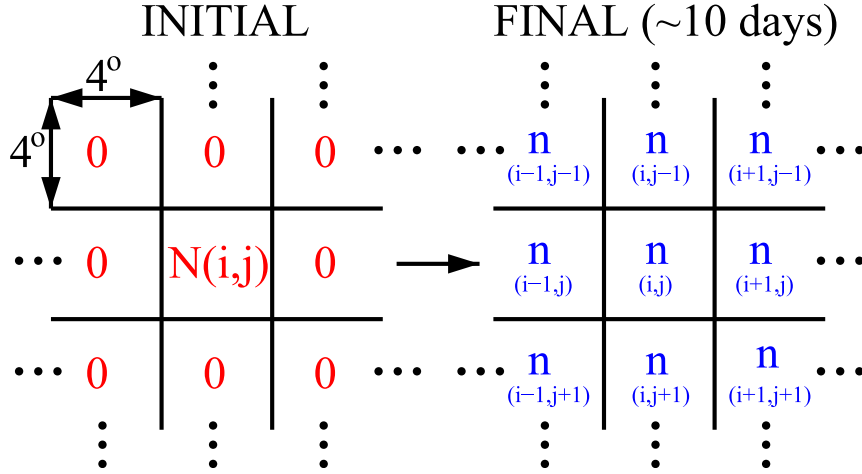


FIG. 1. Methodology to estimate the transfer matrix (\mathbf{M}) and the propagator (\mathbf{H}) of the tracer's density.

the number of floats found in the final boxes over the number of floats initially in the (i_0, j_0) box, that is, the transition probability $n(i, j)/N(i_0, j_0)$.

As an illustration, and to help understand the construction of the 4050 \mathbf{M}_{i_0, j_0} matrices, let us define the (12×12) matrix for the initial cell (with index $2 + 1 \times 4$) within the 12-cell hatched region outlined in Fig. 2:

$$\mathbf{M}_{i_0, j_0} = \begin{pmatrix} 0 & 0 & 0 & 0 & 0 & 0 & 0 & 0 & 0 & 0 & 0 & 0 \\ 0 & 0 & 0 & 0 & 0 & 2/132 & 0 & 0 & 0 & 0 & 0 & 0 \\ 0 & 0 & 0 & 0 & 0 & 1/132 & 0 & 0 & 0 & 0 & 0 & 0 \\ 0 & 0 & 0 & 0 & 0 & 0 & 0 & 0 & 0 & 0 & 0 & 0 \\ 0 & 0 & 0 & 0 & 0 & 11/132 & 0 & 0 & 0 & 0 & 0 & 0 \\ 0 & 0 & 0 & 0 & 0 & 107/132 & 0 & 0 & 0 & 0 & 0 & 0 \\ 0 & 0 & 0 & 0 & 0 & 3/132 & 0 & 0 & 0 & 0 & 0 & 0 \\ 0 & 0 & 0 & 0 & 0 & 0 & 0 & 0 & 0 & 0 & 0 & 0 \\ 0 & 0 & 0 & 0 & 0 & 0 & 0 & 0 & 0 & 0 & 0 & 0 \\ 0 & 0 & 0 & 0 & 0 & 7/132 & 0 & 0 & 0 & 0 & 0 & 0 \\ 0 & 0 & 0 & 0 & 0 & 1/132 & 0 & 0 & 0 & 0 & 0 & 0 \\ 0 & 0 & 0 & 0 & 0 & 0 & 0 & 0 & 0 & 0 & 0 & 0 \end{pmatrix}. \quad (1)$$

Reproducing this calculation for each individual pair of indices (i_0, j_0) , we can define the total transfer matrix as

$$\mathbf{M} = \sum_{i_0, j_0} \mathbf{M}_{i_0, j_0}. \quad (2)$$

We now have a statistical model of the evolution of the float density (or, in other words, of the float repartition) after 10 days, given an initial density. Indeed,

$$\boldsymbol{\rho}(t = 10 \text{ days}) = \mathbf{M}\boldsymbol{\rho}(t = 0), \quad (3)$$

where $\boldsymbol{\rho}$ (a 4050×1 column vector) is the tracer density. In effect, this is the 10-day transition probability matrix or transfer matrix. The propagator of the tracer density can be generalized to

$$\boldsymbol{\rho}(t + \tau) = \mathbf{H}(\tau)\boldsymbol{\rho}(t), \quad \text{where} \quad \mathbf{H}(\tau) = \mathbf{M}^k \quad (4)$$

with $\tau = k \times 10$ days and $k \in N$ is the number of 10-day probabilistic transitions.

Because of the typical ~ 10 -day cycle of Argo floats, the tracer density can only be given every 10 days. Through (4), we have an empirical statistical model of tracer displacements near 1000 m depth, based on the likelihood of Argo float average dispersion during their drift at depth. This assumes a stationary tracer dispersion, since all the floats that happened to be in a given $4^\circ \times 4^\circ$ box are used in the statistics (whatever their times of presence within the box).

It is important to acknowledge that our probabilistic approach allows us to deal with dataset restriction in regard to current knowledge of turbulence and Lagrangian tracer evolution. Indeed the dataset can only describe a “memoryless” system since Argo float trajectories are reset by Argo floats sinking and surfacing on a 10-day time scale. This time scale was chosen following the Lagrangian integral time scale, as inferred from many acoustic float experiments with daily positioning at intermediate depths (from 700 to 1500 m; Freeland et al. 1975; Rossby et al. 1983; Owens 1991; Ollitrault and Colin de Verdière 2002), making Argo float displacements by the mesoscale turbulence a good approximation to random walks. On the other hand, Berloff et al. (2002) and Berloff and McWilliams (2002, 2003) have challenged the view that Lagrangian trajectories only depend of the current particle position (and not of past events). Hence, to reconcile these two issues,

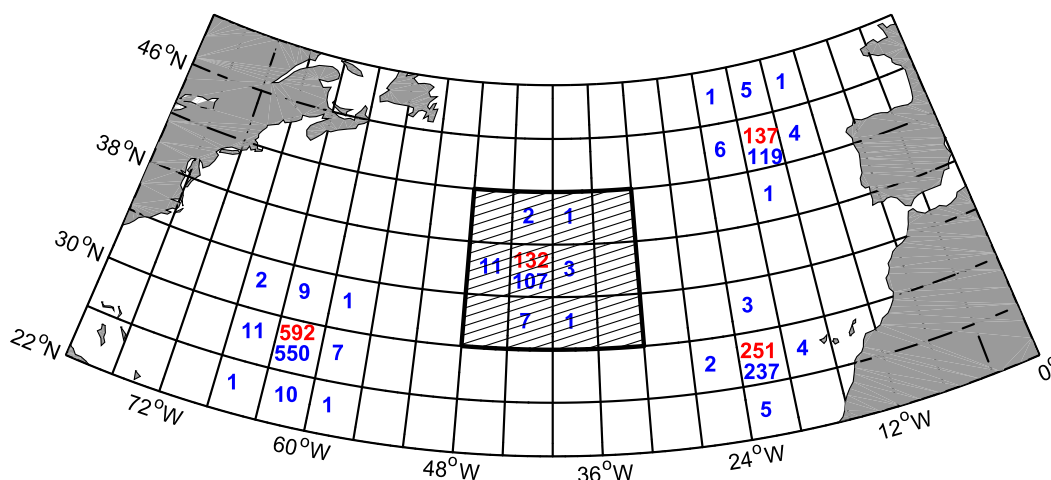


FIG. 2. Four examples of the initial number of floats in a grid cell (N , red numbers) and their repartition after their deep journey (n , blue numbers) following the definition of Fig. 1 and using the ANDRO dataset. Dividing the final number of floats in each grid cell (n) by the initial numbers for a given grid cell (N) gives the likelihood of tracers to go from the initial grid cell to each grid cell in 10 days. The hatched region corresponds to the example used in (1) to illustrate the methodology.

deviations from a Markovian chain (using only particle positions) are simply aggregated in the probabilistic approach of our statistical model.

To summarize, by using the transfer operator approach, it is the advection operator that is transporting the probabilistic properties. This method differs but can be related to another typical method used in Lagrangian particle tracking, where particle motions are derived from the deterministic advection of individual particles using velocity from ocean model or ocean reanalysis. The probability is then evaluated from the statistics of a large set of particle motions. This method has been applied, for example, to two water masses below and above the AAIW: the Antarctic Bottom Water (Jones et al. 2016) and Subantarctic Mode Water (van Seville et al. 2013), respectively.

The philosophy behind this empirical statistical model is equivalent to the one used by van Seville et al. (2012) for oceanic surface drifters. Using Lagrangian tracers to determine the flow properties of the ocean has been applied in a vast domain of oceanography studies from investigation of coherent structures to debris tracking (e.g., Froyland et al. 2007; Dellnitz et al. 2009; van Seville et al. 2011; Maximenko et al. 2012; Froyland et al. 2014).

b. The ANDRO dataset

To compute the matrix \mathbf{M} of Lagrangian tracers, we used an Argo-based deep displacement dataset, the ANDRO dataset (freely available at <http://www.umr-lops.fr/Donnees/ANDRO>). For details on the ANDRO dataset, we refer the reader to Ollitrault and Rannou

(2013), Ollitrault and Colin de Verdière (2014), and Colin de Verdière and Ollitrault (2016). The ANDRO dataset gives access to $\sim 612\,000$ displacements prior to 1 January 2010. This dataset eliminates or corrects parking pressure problems and contains representative and validated parking pressures (generally an average of the measured values during float drift at depth and for every cycle). In particular, the dataset gives easy access to the last known position before sinking, the first known position after surfacing, and their respective times (i.e., dated longitude and latitude before sinking and after surfacing). This allows us to estimate tracer displacements during their drift at depth.

The first step was to restrict displacements that were carried over ~ 10 days and at ~ 1000 dbar (Fig. 3). This reduces the total number of displacement to $\sim 361\,000$.

Now that we have a consistent set of displacements, the methodology described in the previous section can be applied (recall this assumes stationarity of turbulent dispersion and of the general ocean circulation). However, there are still a few sources of error:

- Parking pressures are selected within the range [950, 1150] dbar. However, most of the displacements occur close to 1000 dbar, with a standard deviation of only 28 dbar (Fig. 3). Thus, we assume this error is negligible.
- Drifting time periods at depth (Δt_{deep}) are estimated as the differences between t_i and t_f (the last position time before sinking and the first position time after surfacing, respectively). They are selected in a finite range of [8, 12] days with a standard deviation of only

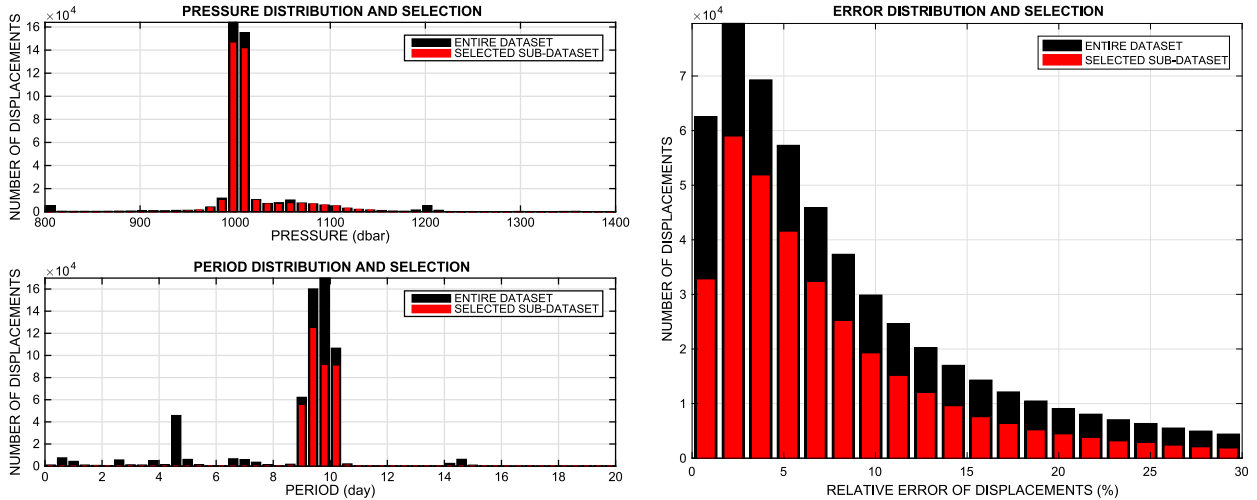


FIG. 3. Distributions of (top left) pressure, (bottom left) period, and (right) relative displacement error of Argo float deep displacements. Distributions are estimated from the entire ANDRO dataset (black) and after selecting displacements at a pressure between 950 and 1100 dbar and with a period from 8.5 to 10.5 days (red). There are $\sim 361\,000$ displacements after selection.

0.42 days (Fig. 3). In the following, we will consider that periods are of 10 days exactly.

- However, since both t_i and t_f are determined at the surface, the actual drift at depth will be biased because of the current shear near the ocean surface. This leads to an error of a few kilometers (less than 5 km for 90% of the displacements) that is estimated in ANDRO, using both the surface and deep approximate velocities (Ollitrault and Rannou 2013). There is also on average an error of 1–2 km due to delays on order of 1 h between the last surface position time and the diving time or between the surfacing time and the first surface position time (most floats are positioned by the Argos satellite system). In conclusion, we can assume on average a possible error on an individual displacement of 5 km. However, this error remains small compared to typical displacements (Fig. 3). More precisely, we find that the expected relative error is below 12%, with 75% of displacements having a relative error below 10%. These errors will be used to estimate the robustness of the results in the rest of the study.

Before using the model, it is important to look at the density coverage of Argo floats, as well as to acknowledge the typical deep displacement of Argo floats. The density of selected Argo floats just prior to their sinking at depth $N(i, j)$ and right after their first surfacing $\tilde{N}(i, j)$ are strongly similar (Fig. 4, top left versus right). This is consistent with an overall weak displacement of tracers over the 10-day drift for our $4^\circ \times 4^\circ$ grid. Looking at the difference between the two distributions, we can see that only a maximum of 10% of tracer density has changed after 10 days (Fig. 4, bottom), but tracer density changes

occur everywhere in the ocean. The distributions are, however, inhomogeneous: there is relative under-sampling in the Southern Ocean and relative over-sampling in the Pacific and the Atlantic, especially in the tropical regions of the Atlantic (in both hemispheres).

Finally, to avoid no-sampling bias, only boxes with at least one tracer before and after one cycle are retained in the analysis, that is, $N(i, j) > 1$ and $\tilde{N}(i, j) > 1$. This leads to an average number of 175 floats per grid cell.

Despite being inhomogeneous, the distribution remains relatively uniform (Fig. 4). The relative difference remains below a factor of 5 in more than 90% of the ocean (40% for a factor of 2). Hence the uniform $4^\circ \times 4^\circ$ grid keeps uniformly reliable statistics. Other strategies exist to keep the number of floats even more uniform by using an adaptive binning approach (e.g., Koszalka and LaCasce 2010; Chen et al. 2014), which is not required here.

c. Error estimation

To estimate the error discussed above in the computation of the 10-day transition matrix, we follow the Monte Carlo method. We build 10 sets of float positions before and after their deep 10-day journey; these positions differ by the addition of a random error (following a centered normal distribution). The intensity of the random error (i.e., the standard deviation of the normal distribution) follows the relative errors estimated for deep displacements available in the ANDRO dataset. Hence, by reproducing the method described in the previous subsection for the 10 sets of positions, we are able to create 10 other transition matrices, their differences representing the uncertainty in the float positions.

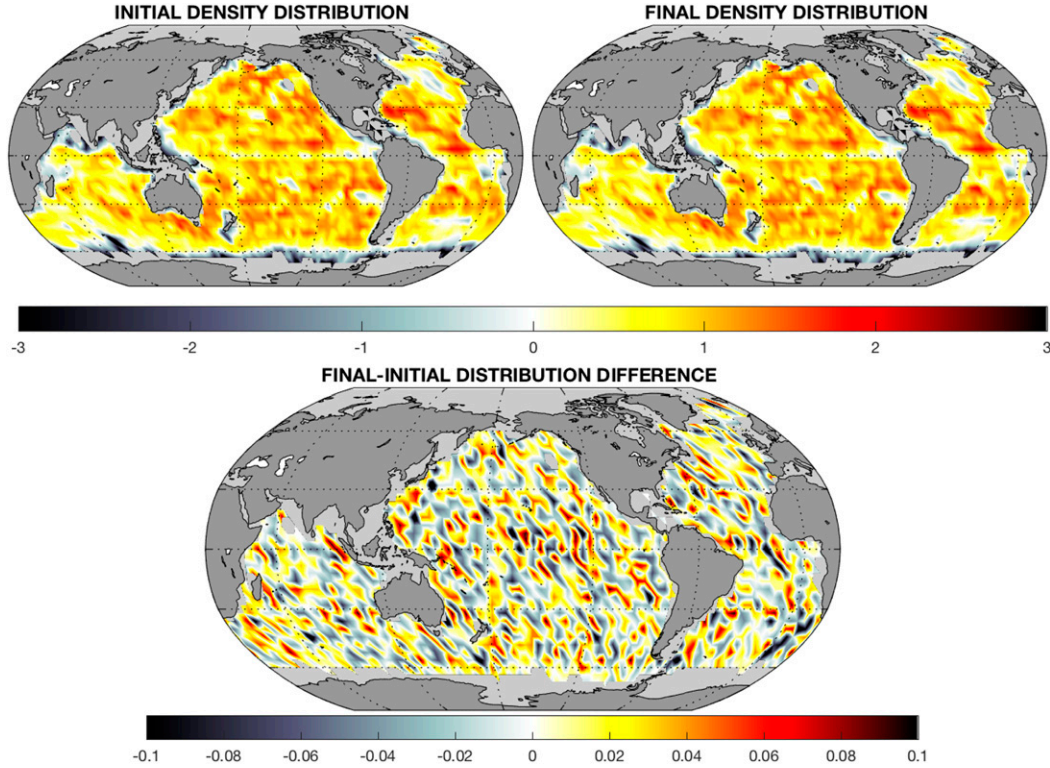


FIG. 4. (top left) Initial and (top right) final (i.e., 10 days after the initial) density distribution of Argo floats. The initial and final distributions $[N(i, j)]$ and $[\tilde{N}(i, j)]$, respectively, are plotted in reference to the global mean distribution (\bar{N}): $\ln[N(i, j)/\bar{N}]$ and $\ln[\tilde{N}(i, j)/\bar{N}]$, where \ln is the natural logarithm function. Positive and negative values correspond to local distribution higher and lower than the mean value, respectively. (bottom) Difference between the initial and final distributions: $[\tilde{N}(i, j) - N(i, j)]/\bar{N}$. Positive and negative values correspond to the region where the distribution increases and decreases over the 10 days, respectively.

To acknowledge the discrepancy between the 10-day transition matrices of the 11 Monte Carlo simulations, we define the transitions matrices as \mathbf{M}_p , their mean as $\mathbf{M} = (1/m) \sum_{p=1}^m \mathbf{M}_p$ (where $m = 11$ is the number of Monte Carlo simulations), and their deviation from this mean as \mathbf{E}_p . Thus,

$$\boldsymbol{\rho}(t + \tau) + \mathbf{e}_p(\tau) = \boldsymbol{\rho}_p(t + \tau) = \mathbf{M}_p^k \boldsymbol{\rho}(t) = (\mathbf{M} + \mathbf{E}_p)^k \boldsymbol{\rho}(t), \quad (5)$$

where $\boldsymbol{\rho}_p(t + \tau)$ is the density after time τ for the matrix \mathbf{M}_p and \mathbf{e}_p is the density deviation.

We can estimate the error on the density field as the standard deviation of $\boldsymbol{\rho}_p(t + \tau)$, or

$$\mathbf{e}(\tau) = \sqrt{\frac{1}{m} \sum_{p=1}^m [\mathbf{e}_p(\tau) \circ \mathbf{e}_p(\tau)]}, \quad (6)$$

where \circ represents the Hadamard product (or the element-wise product).

Assuming that the deviation of the transition matrices is much smaller than their mean (Fig. 3) and $k \geq 1$, we can estimate from (5) the deviation from the mean density field as

$$\mathbf{e}_p(\tau) \simeq \sum_{l=0}^{k-1} (\mathbf{M}' \mathbf{E}_p \mathbf{M}^{k-1-l}) \boldsymbol{\rho}(t). \quad (7)$$

Here all the powers of \mathbf{E}_p greater than one have been neglected. Note that for $k = 1$, this expression is not an approximation, but is exact. Also, in this last framework, the expression (4) remains valid, but expresses the mean solution [since $(1/m) \sum_{p=1}^m \mathbf{e}_p(\tau) = 0$].

From these expressions we can see that the deviation from the mean is a function of the initial density field $\boldsymbol{\rho}(t)$ and the length of the experiments k . From (5) and (7), the relative deviation $\mathbf{e}_p(\tau)/\boldsymbol{\rho}(t + \tau)$ scales as $k\mathbf{e}_p(10 \text{ days})/\boldsymbol{\rho}(t + 10 \text{ days})$. Hence, to illustrate the error, we choose a simple case where $\boldsymbol{\rho}(t)$ is a uniform density distribution and $\tau = 1$ year. Using (6), we find that the relative error has a median value of $24\% \text{ yr}^{-1}$ (Fig. 5). This suggests that long time scale (>4 years) results might be quite speculative in general. Hence, in this study, an error estimate will be provided for all specific results. As discussed in more detail in section 3, long time scale and asymptotic results of this study are robust, despite some second-order quantitative changes.

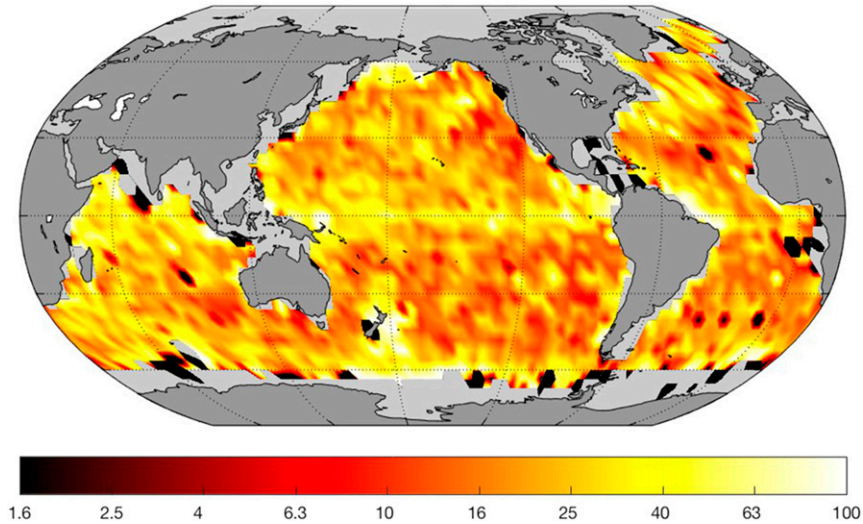


FIG. 5. Error estimation ($\% \text{ yr}^{-1}$) for an initial uniform distribution, following the discrepancy in 10-day transition matrices from the 11 Monte Carlo simulations. The median value of the error is of $24\% \text{ yr}^{-1}$. This error estimate suggests that any quantitative result beyond 4 years is highly speculative, that is, more than half of the data will have relative errors bigger than 100%.

3. Results

a. Evolution toward asymptotic behavior

Now that the model has been described, implemented with the ANDRO dataset and general error estimated, we use long time integration to better understand the key characteristics of our empirical statistical model. For this purpose we initialize the tracer density (ρ) uniformly and describe its evolution toward asymptotic behavior.

Before looking at this evolution, it is important to acknowledge that setting a uniform tracer field as the initial condition is not a trivial choice. Indeed, using a simple 2D advection–diffusion equation for the evolution of tracer density and assuming a Laplacian operator for diffusion, the evolution of tracer density reads

$$\partial_t \rho + \partial_x(u\rho) + \partial_y(v\rho) = \partial_x(k_x \partial_x \rho) + \partial_y(k_y \partial_y \rho), \quad (8)$$

where x and y are the two horizontal coordinates; ρ is the local tracer density (a function of x and y); u and v are the x and y velocities (here, these velocities represent both the mean flow and the eddy induced one); and k_x and k_y are horizontal diffusivities, respectively. Hence, using 3D nondivergence ($\partial_x u + \partial_y v + \partial_z w = 0$, where z is the vertical coordinate and w the z velocity), we have

$$\partial_t \rho + u \partial_x \rho + v \partial_y \rho = \partial_x(k_x \partial_x \rho) + \partial_y(k_y \partial_y \rho) + \rho \partial_z w. \quad (9)$$

At the initial time, the uniform tracer density ($\partial_x \rho = \partial_y \rho = 0$) implies

$$\partial_t \rho = \rho \partial_z w. \quad (10)$$

Hence, the very existence of an evolution of the tracer density from a uniform initial density comes from the divergence of the horizontal velocity field. This suggests that the uniform density (i.e., the “well mixed” case) is not an equilibrium solution because of horizontal divergence.

Starting from this uniform density field, the time evolution of the density field shows four regimes. In the first regime (~ 1 yr), the tracer density seems to randomly evolve and the signal has the property of white noise (Fig. 6a), that is, all the spatial scales have the same signature. In the second regime (~ 10 yr), a clustering of the density appears with the selection of large scales (Fig. 6b). The spectral signature is more red but remains typical of noise. In the third regime (~ 100 yr), the clustering is even more obvious, with a few large regions concentrating most of the initial uniformly distributed tracers (Fig. 6c). These regions are mainly centered in the subtropical gyres recirculation (west of the North and South Atlantic and North Pacific, as well as east of the North and South Pacific). Finally, in the fourth regime (~ 1000 yr), the tracer density converges to a few points in the ocean (Fig. 6d): floats are trapped there. The rest of the ocean is devoid of tracers.

This regime change shows how long it takes for the large-scale circulation to imprint the tracer evolution. In the first few years, the tracers are almost submitted to a random walk, whereas on longer time scales, decades to centuries, the mean flow plays a more significant role forcing the tracers to cluster in regions of convergence at ~ 1000 m. The existence of stationary points is of particular importance since it suggests a fate of floats.

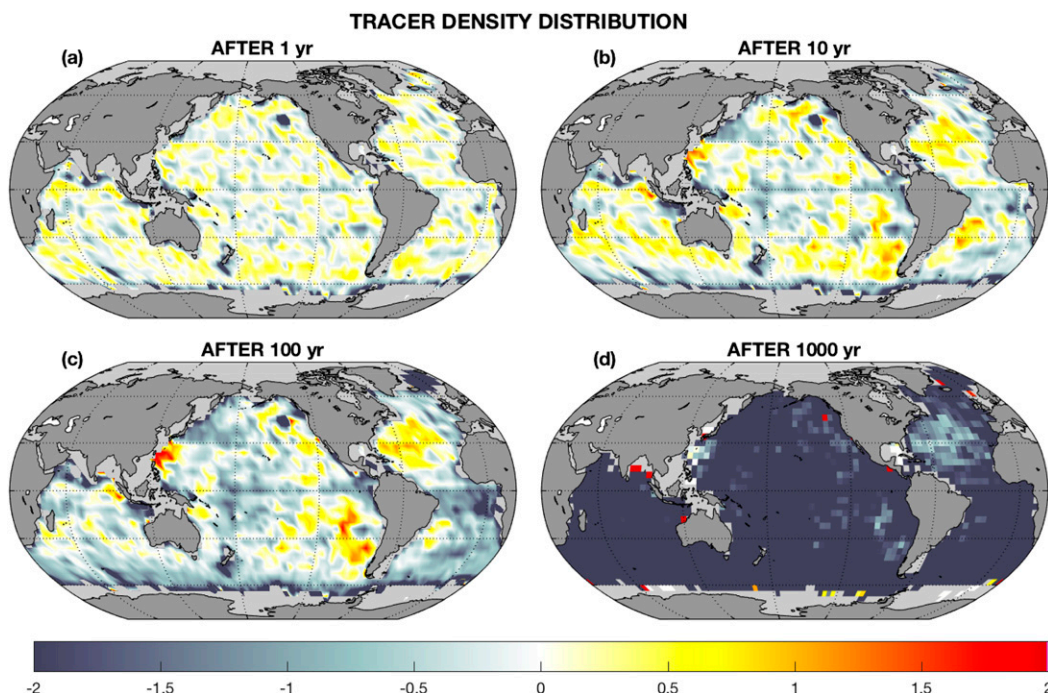


FIG. 6. Distribution of tracers $\{\ln[\rho(t)]\}$ after $t =$ (a) 1, (b) 10, (c) 100, and (d) 1000 years, computed with the Lagrangian statistical model starting from a uniform distribution. Positive and negative values represent increase and decrease of the distribution, respectively. Purple corresponds to maximum positive values to highlight locations of high convergence (i.e., asymptotic stationary points).

Indeed, any float would reach and remain at these locations eventually.

The exact locations of the stationary points can be obtained by extracting the locations with a relative attractivity bigger than 1% asymptotically, that is, the locations where more than 1% of the initially uniformly distributed tracers converge. We found such 10 locations: 1) the East China Sea, containing 29% of tracers asymptotically [above 3 kyr (1 kyr \equiv 1000 years)]; 2) off the coast of Vancouver Island, 18%; 3) the Bay of Bengal, 12% (distributed over three close regions: west contributing 29%, central 28%, and east 43%); 4) Cooperation Sea (close to Antarctica), 12%; 5) along the coast of California, 9.6%; 6) along the coast of Central America, 6.2%; 7) the southern tip of Chile, 4.6%; 8) along the northwest coast of Australia, 2.2%; 9) the Riiser-Larsen Sea, 1.8%; and 10) the Iceland Sea (north of Iceland), 1.8% (Fig. 7a). These 10 locations, representing less than 1% of the ocean surface, contain more than 97.5% of the tracers asymptotically.

These stationary points are extremely robust across the 11 Monte Carlo simulations defined in section 2c and used to estimate the impact of the observational errors (Fig. 8). Over the 11 simulations, 9 of the 10 stationary points are always present, 1 is there 65%, and 2 new stationary points can be identified but are only marginally

robust, being present only 25% and less than 10% over the ensemble, and are ignored in the rest of the analysis. Beyond the robustness of their existence, their attractivity is also robust across tested simulations, with the standard deviation of their attractivity always remaining significantly below the mean value (Table 1).

The convergence to this asymptotic statistical distribution is on the order of 1000 yr (Fig. 7b, Table 1). This suggests that in ~ 1000 yr floats will have reached their final destination (i.e., one of the stationary points). This gives a typical adjustment time scale for the deep ocean that is consistent with numerical model results (Wunsch and Heimbach 2008; Siberlin and Wunsch 2011; Sévellec and Fedorov 2016). To further describe the adjustment time scales, tracer convergence to a given stationary point is fitted with an exponential law of the form: $C = C_0[1 - \exp(-t/\tau)]$, where C (C_0) is the (final) percentage of tracers attracted by stationary point and τ is the typical convergence time scale. We define ΔC_0 as the standard deviation of C_0 over the 11 Monte Carlo simulations. We can also estimate the asymptotic convergence time scale (T_∞) corresponding to the minimum time when $(C_0 - C)/C_0$ is smaller than 1%. (Results are summarized in Table 1.) This analysis suggests that, whereas the full convergence takes on the order of 1000 yr, typical convergence time scales are on the order of a few hundred years.

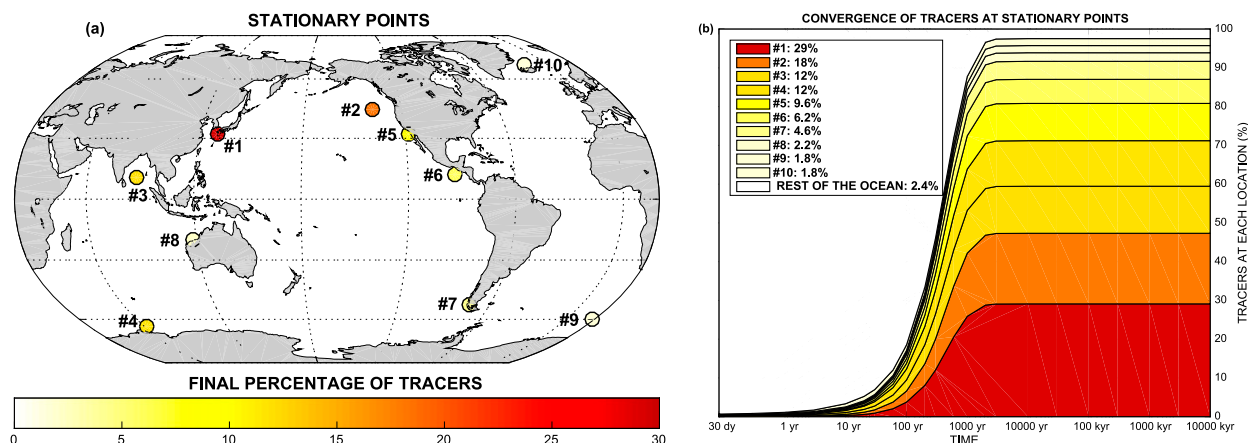


FIG. 7. (a) Location of the 10 main stationary points (i.e., location with a final convergence bigger than 1%). The relative attractivity of each stationary point is given by the color scale, that is, final percentage of tracers located at the particular stationary point. (b) Convergence of the tracers to the 10 main stationary points. The permanent regime is achieved at ~ 3 kyr. These 10 locations attract more than 97.5% of all tracers. Color scale gives the final percentage at each location as in (a).

b. Asymptotic attractors

Refining this global analysis to a local one reveals striking differences in the attractivity of the 10 main stationary points. To demonstrate this, we independently initialize each of the 2056 individual oceanic $4^\circ \times 4^\circ$ grid cells and compute their asymptotic behavior, that is, the percentage of tracers ending up in each of the 10 main stationary points. These experiments allow us to map where the tracers ending up in each of the 10 main stationary points come from,

in a statistical sense (i.e., a particular location can feed several stationary points). Hence, it shows the attractor basin of the stationary points, or their asymptotic attractivity (Fig. 9).

This analysis reveals three subgroups of stationary points (Fig. 9). For 1–6, the attractivity is global, despite regional change in the intensity of the attractivity. From 7–9, the attractivity excludes the North Pacific. Stationary point 10 (not shown) is a purely regional attractor and attracts exclusively but totally tracers from the Arctic (because of bathymetry constraints). This explains its

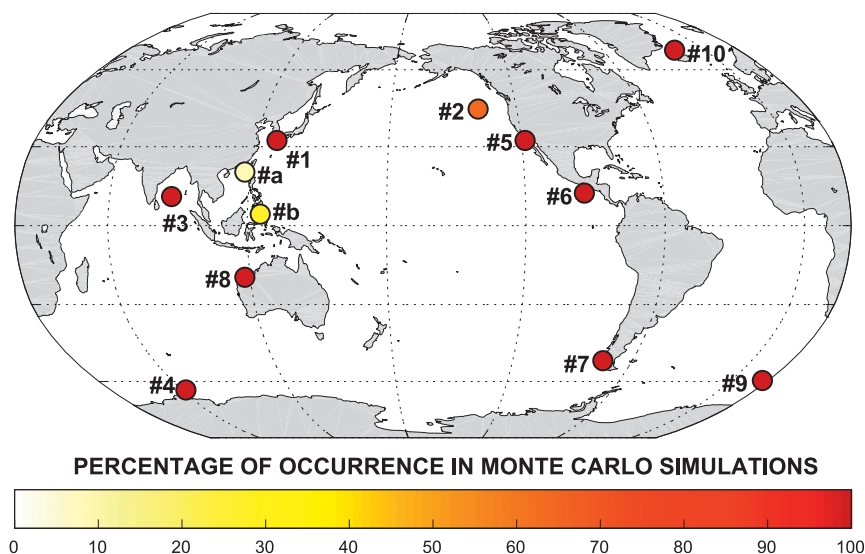


FIG. 8. Robustness of the 10 main stationary points across the 11 Monte Carlo simulations used to estimate the impact of observational errors. The color indicates the percentage of occurrence of the stationary points over the 11 simulations. Two new stationary points (a and b) have been identified but with a weak robustness.

TABLE 1. Characteristics of the tracer convergence to stationary points.

| Stationary points | Global | | | | NPIW | | | | MW | | | | AAIW | | | |
|------------------------------|-----------|------------------|-------------|------------------|-----------|------------------|-------------|------------------|-----------|------------------|--------------|------------------|-----------|------------------|-------------|------------------|
| | C_0 (%) | ΔC_0 (%) | τ (yr) | T_∞ (kyr) | C_0 (%) | ΔC_0 (%) | τ (yr) | T_∞ (kyr) | C_0 (%) | ΔC_0 (%) | τ (kyr) | T_∞ (kyr) | C_0 (%) | ΔC_0 (%) | τ (yr) | T_∞ (kyr) |
| 1) East China Sea | 29 | 11 | 510 | 3 | 56 | 19 | 240 | 2 | 23 | 11 | 2.0 | 10 | 24 | 9.0 | 730 | 3 |
| 2) Coast of Vancouver Island | 18 | 8.2 | 490 | 2 | 26 | 11 | 280 | 2 | 14 | 11 | 2.0 | 10 | 15 | 6.7 | 710 | 2 |
| 3) Bay of Bengal | 12 | 3.5 | 390 | 2 | 1.9 | 1.2 | 790 | 3 | 17 | 7.0 | 1.3 | 3 | 15 | 4.6 | 400 | 2 |
| 4) Cooperation Sea | 12 | 2.2 | 390 | 2 | 2.3 | 1.5 | 700 | 2 | 20 | 6.4 | 1.2 | 3 | 18 | 2.7 | 330 | 2 |
| 5) Coast of California | 9.6 | 3.1 | 490 | 2 | 9.4 | 3.4 | 350 | 2 | 7.8 | 4.6 | 2.0 | 10 | 8.4 | 2.8 | 640 | 2 |
| 6) Coast of Central America | 6.2 | 2.9 | 440 | 2 | 2.4 | 1.1 | 480 | 2 | 6.2 | 9.2 | 1.6 | 3 | 6.8 | 2.9 | 470 | 2 |
| 7) Southern tip of Chile | 4.6 | 1.4 | 410 | 2 | 1.1 | 0.86 | 640 | 2 | 6.5 | 3.1 | 1.3 | 3 | 7.2 | 2.1 | 340 | 2 |
| 8) Coast of Australia | 2.2 | 0.64 | 350 | 2 | 0.35 | 0.29 | 800 | 2 | 2.9 | 2.1 | 1.3 | 3 | 2.8 | 0.75 | 360 | 2 |
| 9) Riiser-Larsen Sea | 1.8 | 0.38 | 380 | 2 | 0.37 | 0.25 | 670 | 2 | 3.2 | 1.0 | 1.2 | 3 | 2.8 | 0.49 | 330 | 2 |
| 10) Iceland Sea | 1.8 | 0.25 | 22 | 2 | ~0 | ~0 | — | — | ~0 | ~0 | — | — | ~0 | ~0 | — | — |

relatively short typical convergence time scale of 22 yr. It is also interesting to note that the attractivity of stationary points 1 and 2, and to a weaker extent 3 and 4, is huge. For instance, stationary point 1 attracts more than 50% of the Pacific tracers and up to one-third of the other regions. Equivalently, stationary point 2 attracts almost all of the rest of Pacific tracers (especially in the North Pacific) and a significant fraction of the tracers from the rest of the ocean. This leaves only a relatively weak fraction of the tracers to the other eight main stationary points. This result is consistent with the global analysis (Fig. 7).

Interestingly, the attractivity of the stationary points is a smooth function of longitude and latitude, especially when compared to previous global analysis (Fig. 6). This, to some extent, suggests the relevance of the decomposition in terms of stationary points. It is the competing attractivity of the 10 stationary points that induces the relatively noisy response of the system. However, the individual basins of attraction, even if defined in a statistical sense, are smooth.

4. Application to 1000-m water masses

Now that we have fully developed the model and described its asymptotic behavior, we can use it to describe the fate of the three typical water masses that are injected around 1000 m, the relevant depth for the empirical statistical model. These three water masses are the North Pacific Intermediate Water, which enters the North Pacific through the Kuril Islands chain; the Mediterranean Water, which enters the North Atlantic through the Strait of Gibraltar; and the Antarctic Intermediate Water, which reaches 1000 m in the Southern Ocean north of the Polar Front.

The traditional conjecture is that intermediate water masses in the ocean interior flow along isopycnal surfaces and not horizontal surfaces, as the Argo floats do. The two surfaces differ markedly in the formation regions where isopycnals outcrop or in the adjustment area outside the Straits of Gibraltar for the Mediterranean water. Away from these limited regions, in the ocean interior, the intermediate water masses that we consider have typical vertical extensions of 500 m, which is greater than the vertical excursions of isopycnal surfaces [on the order of 50 m, as suggested by Hennon et al. (2014)]. Indeed, the vertical displacement of water parcels can be estimated by $T_{\text{std}}/\partial_z T$, where T_{std} is the time standard deviation of the potential temperature around 1000 m measured by Argo floats and $\partial_z T$ is the mean vertical gradient of potential temperature around 1000 m given by the climatology of the *World Ocean Atlas 2009* (Locarnini et al. 2010). Taking the global mean of this estimate, we find an average vertical displacement of 50 m (after removing displacements bigger

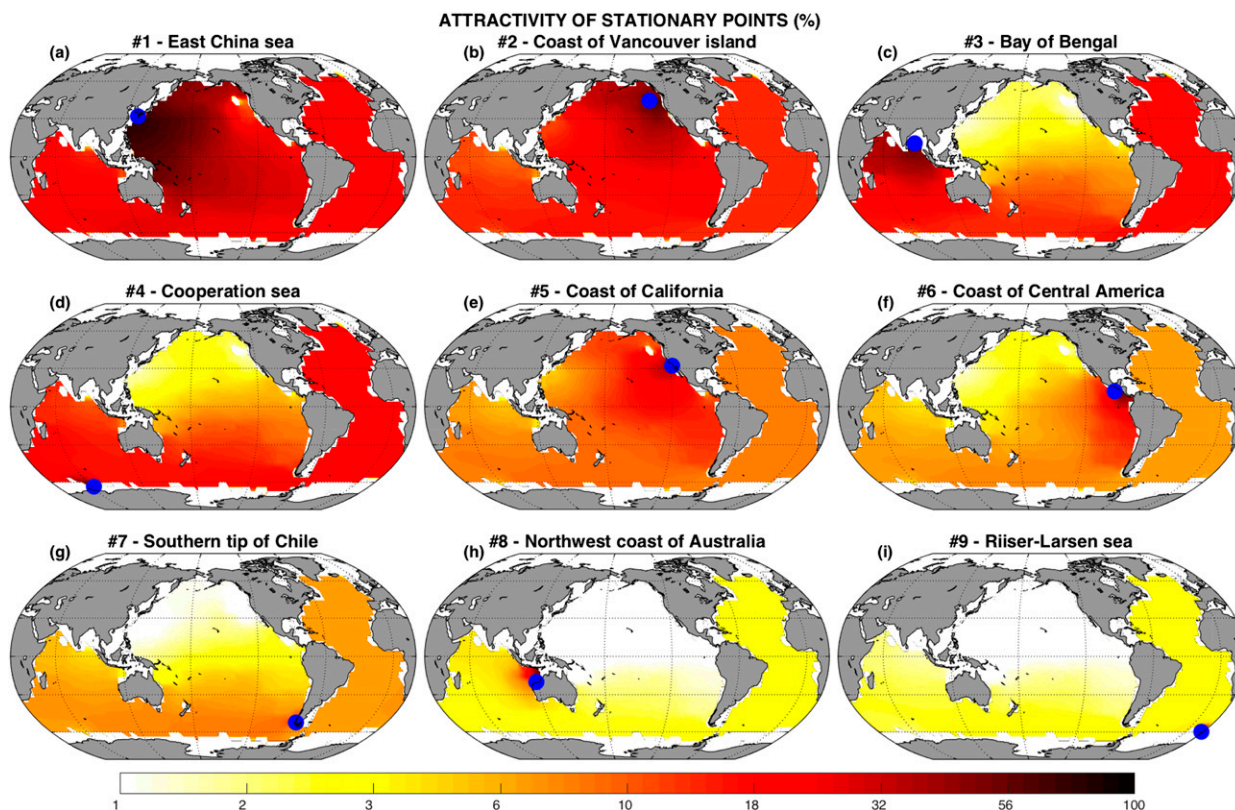


FIG. 9. For each location the percentage of tracers asymptotically converging to a stationary point 1–9, that is, the attractivity. The blue dot indicates the location of the stationary point for which the attractivity is computed. The color bar follows a logarithmic scale visually highlighting low values. (Stationary point 10 is not shown, since it exclusively but totally attracts tracers from the Arctic.)

than 200 m to avoid regions of water mass formation that represent only 7% of the globe). Because these displacements remain small compared to the typical thickness of water masses, our working hypothesis is that the displacement statistics of water parcels are homogeneous over this depth range. Consequently, “depth” and “isopycnal level” are interchangeable in respect to intermediate water masses.

Two experiments are set to understand the fate of these three water masses: an initial value problem (i.e., an initial pulse of tracers) and a boundary condition problem (i.e., continuous forcing of tracers). In the first experiment (the initial value problem), a pulse of tracers is introduced at the 1000-m entry point of the water mass, that is, the Kuril Islands chain for NPIW (Talley 1993; Shcherbina et al. 2003), the Strait of Gibraltar for MW, and the Polar Front for AAIW [following the definition of Orsi et al. (1995)]. As in the previous section, the percentage of tracers ending up at the exact locations of the 10 stationary points is evaluated (Fig. 10), as well as the typical and asymptotic convergence time scales (Table 1).

The second experiment (the boundary condition problem) is closer to what is expected in the ocean. For

each water mass, an almost constant flux of tracers (a pulse every 1 yr) is imposed for 3000 yr (asymptotic/permanent regime, Fig. 10) at the entry point (at 1000 m) of the water mass (Kuril Islands chain, Strait of Gibraltar, and Polar Front for NPIW, MW, and AAIW, respectively). Removing from the analysis the locations of the 10 stationary points (to avoid accumulation to infinity), we evaluate the density of tracers at different time integration intervals (at 3, 30, 300, and 3000 yr, see Fig. 11). This second set of experiments shows highly contrasting results. Indeed, NPIW converges to a local region of the Kuroshio recirculation, MW is concentrated regionally in the subtropical gyre, and AAIW spreads out globally, as expected from more classical analysis of intermediate water (Talley 2008; Talley et al. 2011). Note that this consistency can be considered as an a posteriori validation of our empirical model.

a. Evolution and fate of North Pacific intermediate water

As expected from a source in the North Pacific, given the local analysis result (Fig. 9), most of the tracers initiated

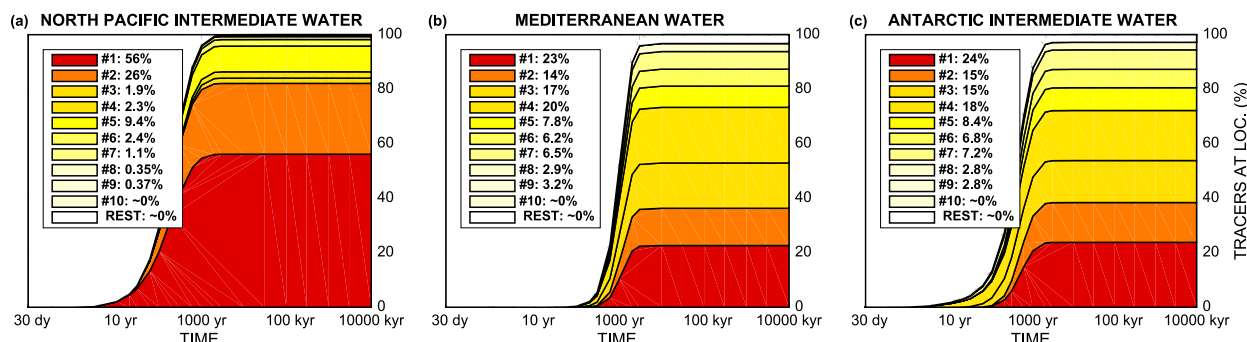


FIG. 10. As in Fig. 7b, but for initial conditions at (a) the Kuril Islands chain, (b) the Strait of Gibraltar, and (c) the Polar Front representing injection of NPIW, MW, and AAIW.

along the Kuril Islands chain are collected by the East China Sea stationary point 1 (up to 56%, Fig. 10a). The coasts of Vancouver Island (point 2) and of California (point 4) are the two other significant asymptotic attractors for the NPIW (with 26% and 9.4%, respectively). The other stationary points only get a weak residual with less than 2.5% at the maximum. This shows that the NPIW ends up mainly in the North Pacific. NPIW reaches full convergence to stationary points in ~ 1000 yr, whereas its typical convergence time scales are multicentennial (Table 1).

The second experiment confirms the results from the first one: NPIW is restricted to the North Pacific and mainly the northwest boundary of the North Pacific (Fig. 11a). Over annual time scales, NPIW is restricted along the Kuril Islands chain, barely progressing in the North Pacific [Fig. 11a(1)]. Over decadal time scales, NPIW has spread along the western and northern Pacific boundaries, and significant traces of NPIW cover half of the North Pacific [Fig. 11a(2)]. On longer time scales (centennial to millennial), the permanent regime shows that there are traces of NPIW all over the northwest part of the North Pacific; however, the tracers are significantly concentrated at a local scale in the recirculation region of the Kuroshio [Figs. 11a(3),a(4)], consistent with observational studies such as those of Talley et al. (1995) and Talley (1993, 1997, 2008).

Despite the long time scales considered in this study, we are not considering any active feedback of water masses in this setup. For example, exchange with the atmosphere or dynamical adjustments (e.g., Rossby waves or convection) are ignored. In this sense, it is only particles that are followed regardless of their possible interactions or property changes (as long as it remains at 1000 m depth).

To clarify the impact of observational errors, we use the 11 Monte Carlo simulations defined in section 2 to compute the error in the fate of NPIW as the standard deviation of the 11 simulations (Fig. 12a). This shows that the errors are negligible on interannual time

scales, remaining below 10% of our estimate [Fig. 12a(1) versus Fig. 11a(1)], whereas on longer time scales the error is more significant, but remains small, with maximum values below 20% for 30 yr [Fig. 12a(2)] and 30% for 300 and 3000 yr [Figs. 12a(3),a(4)]. This analysis also shows that the impact of observational errors follows the NPIW spread estimate for all time scales (Fig. 11 versus Fig. 12). In the same manner, we have estimated the error linked to the choice of the model resolution. To this purpose, we have recomputed all the solutions for two other resolutions ($5^\circ \times 5^\circ$ and $6^\circ \times 6^\circ$) and estimated error induced by the resolution as the standard deviation of the three resolutions (after a nearest interpolation onto the reference $4^\circ \times 4^\circ$ resolution; Fig. 13a). This shows a significant variability between resolutions on interannual time scales at the location of the maximum of the NPIW signal [Fig. 13a(1)]. This error, which remains below the values of the signal, can be interpreted as an error on the exact position of the maximum spread. However, the absence of variability outside the NPIW signal also suggests that the spread of NPIW is still restricted to the same area regardless of the resolution. On longer time scales, the impact of resolution shows the same behavior as on interannual but with a weaker impact [Figs. 13a(2)–(4)]. For example, on centennial and millennial time scales the impact only reached 50% of the NPIW spreading signal.

b. Evolution and fate of Mediterranean water

The Mediterranean Water, despite being initiated in the North Atlantic, finishes its journey in other oceans (Fig. 10b). This is consistent with the local analysis of tracers starting in the North Atlantic (Fig. 9). The two stationary points collecting the highest number of tracers initiated at the Strait of Gibraltar are 1 (East China Sea, 23%) and 4 (Cooperation Sea, 20%). The third and fourth stationary points, collecting up to 17% and 14%, are 3 (Bay of Bengal) and 2 (off the

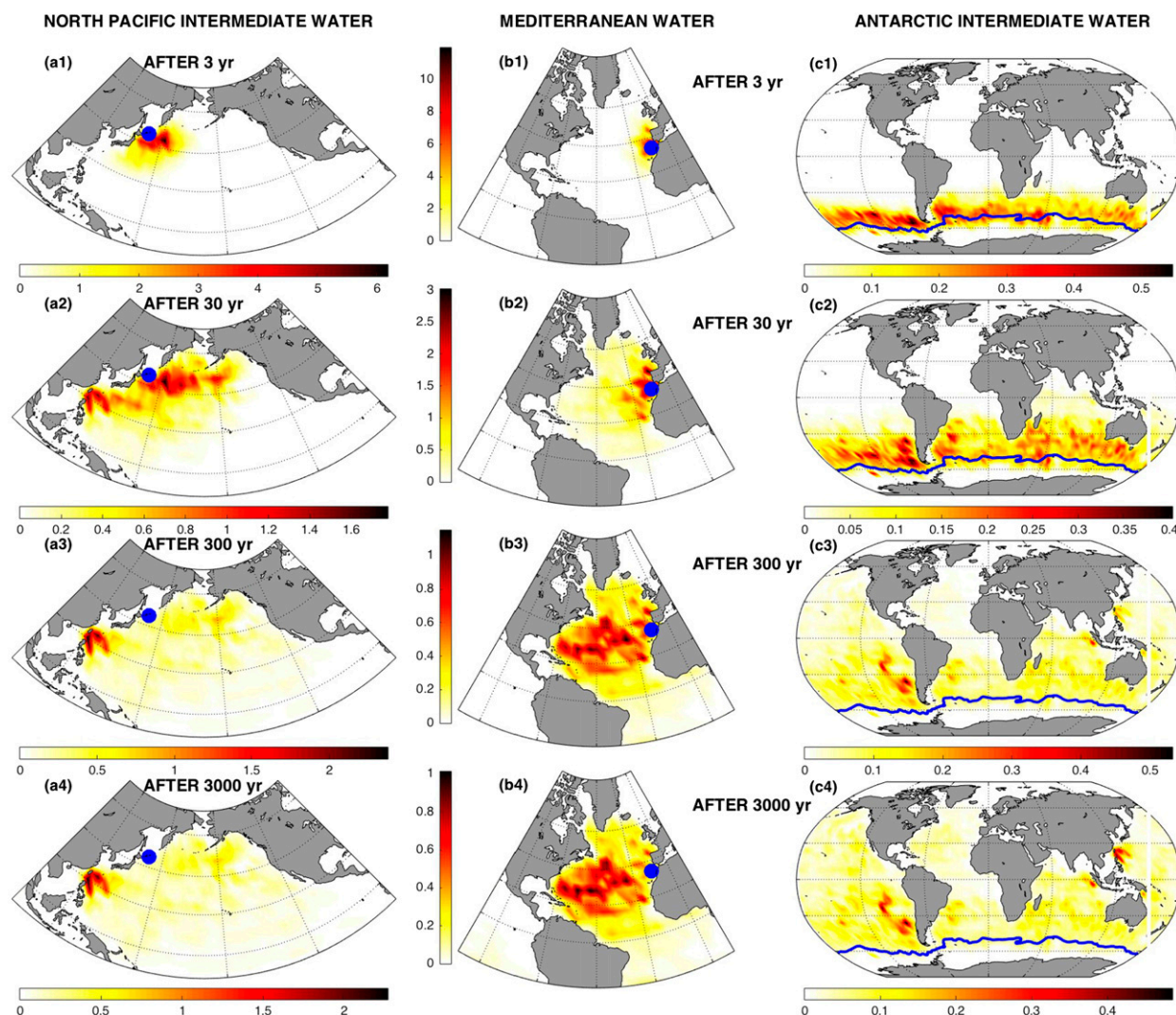


FIG. 11. Density of tracers (%) after 3, 30, 300, and 3000 yr when a constant inflow at (a1–4) the Kuril Islands chain (blue dot), at (b1–4) the Strait of Gibraltar (blue dot), and at (c1–4) the Polar Front (blue line) is imposed in the empirical statistical model. The first source represents NPIW, the second one represents the MW, and the last one represents the AAIW. The last three figures (a4, b4, and c4), corresponding to 3000 years of time integration, are the permanent regime, that is, the density will not further evolve.

coast of Vancouver Island), respectively. These four stationary points together collect more than two-thirds of the MW tracers. The rest is split between stationary points from 5 to 9 with a maximum attraction weaker than 8% (stationary point 10 getting 0% of MW tracers). The asymptotic convergence of MW takes 3000–10 000 yr (Table 1), slightly longer than for the two other starting locations. This is due to the large distance between the source (Strait of Gibraltar) and the most relevant stationary points (locations 1–4). Consistently, the typical convergence time scales are long, of a few thousand years.

Using the second experiment, we test how MW spreads in the ocean when a continuous source of water

is imposed at the Strait of Gibraltar. This experiment shows that on interannual time scales the MW remains in the neighborhood of the Strait of Gibraltar with a nonnegligible fraction moving northward in the Bay of Biscay [Fig. 11b(1)], consistently with observations on the salt tongue of Mediterranean Water into the North Atlantic through Lagrangian float analyses (Spall et al. 1993; Bower et al. 1997, 2002). On multidecadal time scales, this water spreads in the entire North Atlantic [Fig. 11b(2)]. However, it remains mainly in the Bay of Biscay and along the coasts of Portugal and Morocco. On centennial time scales, most of the tracers are trapped in the subtropical gyre of the North Atlantic [Fig. 11b(3)]. In the permanent regime (3000 yr), the

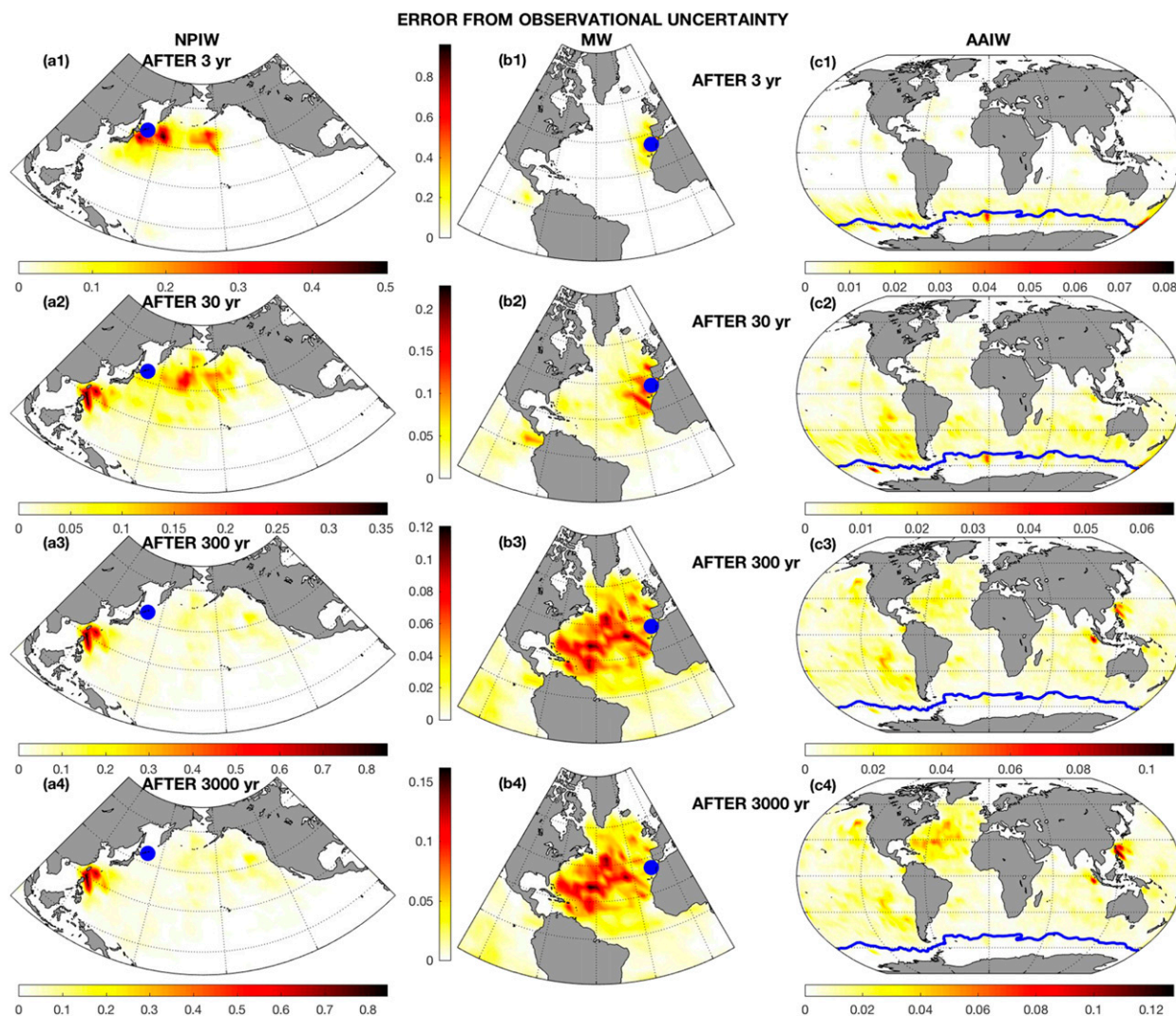


FIG. 12. As in Fig. 11, but for the observational errors estimated as the standard deviation of the 11 Monte Carlo simulations.

tracers are concentrated inside the subtropical region [Fig. 11b(4)]. This result is consistent with previous observational studies of the spread of Mediterranean Water based on its typical water properties by Needler and Heath (1975), Iorga and Lozier (1999a,b), Talley (2008), and van Aken (2000), as well as the numerical analysis of Stanev (1992) and theoretical investigations by Richardson and Mooney (1975) and Stephens and Marshall (1999). The signature of MW at the Strait of Gibraltar is not as intense as on shorter time scales. At this asymptotic time scale, traces of MW can also be found in the entire ocean (including Pacific).

As for NPIW, we used the 11 Monte Carlo simulations to compute the error of the fate of MW (Fig. 13b). This shows that the errors are negligible on all tested time scales, remaining below 10% of our estimate [Figs. 13b(1)–(4) versus Figs. 11b(1)–(4)]. For the errors due

to the resolution, the same conclusion as for NPIW can be drawn. The error remains below the values of the signal and can be interpreted as an error on the exact position of the maximum spread [Figs. 13b(1)–(4)].

c. Evolution and fate of AAIW

The Antarctic Intermediate Water shows a strong convergence toward the North Pacific, with more than half of it asymptotically converging there. Indeed, most of the AAIW reaches the first four stationary points: 24% for 1, 18% for 4, and 15% for 2 and 3 (Fig. 10c). The other attractors capture less than 8.5%. As expected from previous analyses, the Iceland Sea does not attract any AAIW, since it only attracts tracers from the Arctic Ocean. It is interesting to note that, despite there being three stationary points in the Southern Ocean (4, 7, and 9), they only attract 28% of the AAIW. In this experiment

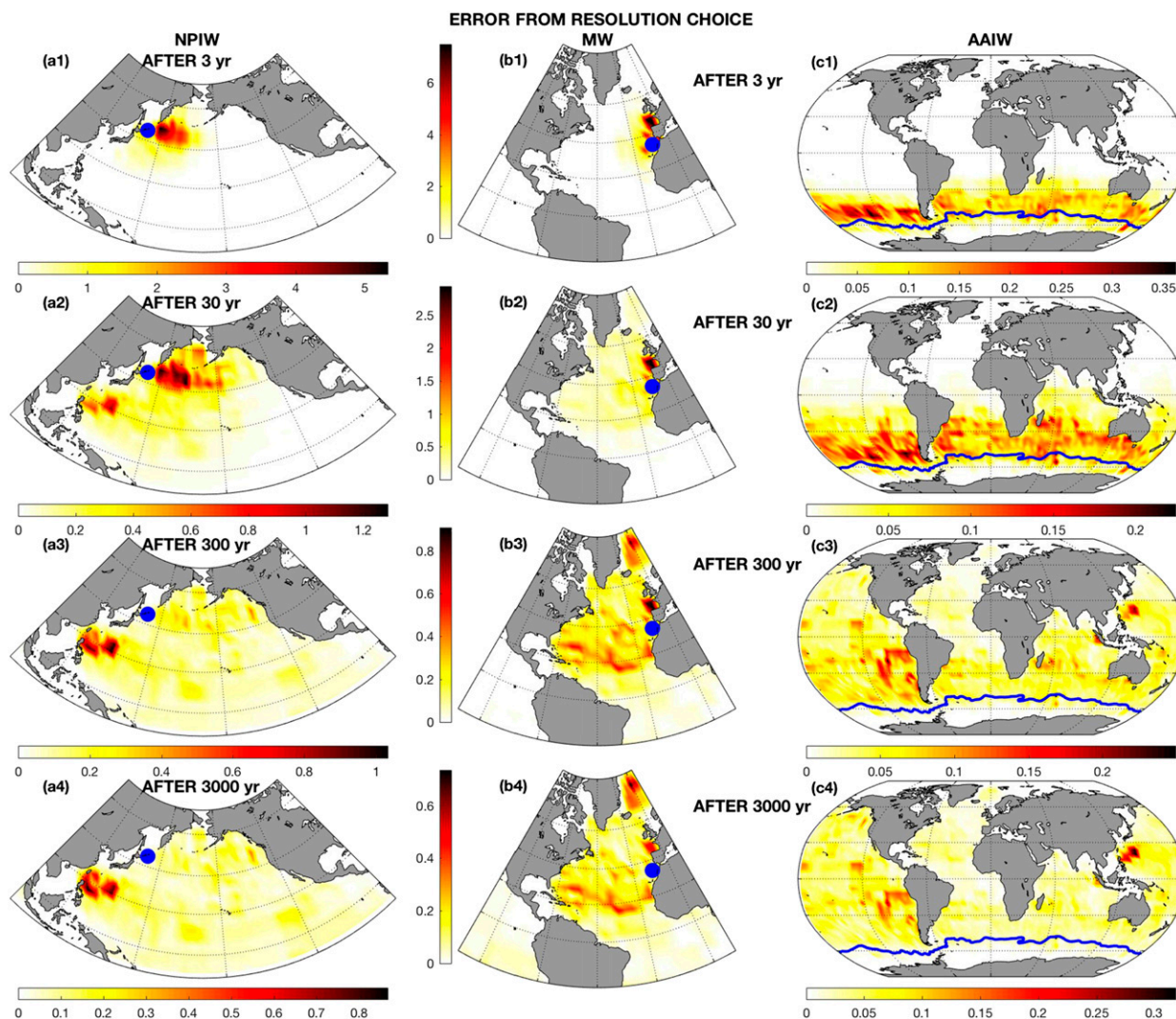


FIG. 13. As in Fig. 12, but for error induced by the choice of model resolution. This error is estimated as the standard deviation between three different uniform resolutions: $4^\circ \times 4^\circ$ (our reference resolution), $5^\circ \times 5^\circ$, and $6^\circ \times 6^\circ$. To diagnose the standard deviation, the two lowest resolutions have been interpolated using a nearest interpolation on the reference resolution ($4^\circ \times 4^\circ$).

equilibrium is reached in ~ 1000 yr, with multicentennial typical convergence time scales (Table 1).

The second experiment (setting a constant flux along the polar front) shows a meridional spread of tracers all over the Southern Ocean on interannual time scales [Fig. 11c(1)]. On decadal time scales, the main signature remains in the Southern Ocean slightly northward of the Polar Front, with incursion in other ocean basins, especially in the Indian Ocean [Fig. 11c(2)]. At centennial time scales, the tracer flux from the Polar Front has reached most of the World Ocean. Its signature is not intensified in the Southern Ocean (its region of origin) but in the Kuroshio recirculation and along the eastern boundary of the Southern Pacific [Fig. 11c(3)]. In the permanent regime (after 3000 yr), NPIW spreads almost evenly globally [Fig.

11c(4)], as previously suggested by Talley (2008). The spread of AAIW in the South Atlantic is consistent with the study of Suga and Talley (1995) and Talley (1996), especially its relative weak signature around the equator [Fig. 11c(4)].

As for the two other intermediate waters, the observational error of the spread of AAIW is estimated through the 11 Monte Carlo simulations (Fig. 13c). For all tested time scales the errors are weak, remaining below 20% [Figs. 13c(1)–(4) versus Figs. 11c(1)–(4)]. For the resolution, unlike NPIW and MW, the error remains below 50%, suggesting the relatively weak impact of resolution for NPIW. Also, since the error remains in the regions of high values of the signal, it can be interpreted as an error on the pattern intensity, rather than the pattern itself [Figs. 13c(1)–(4)].

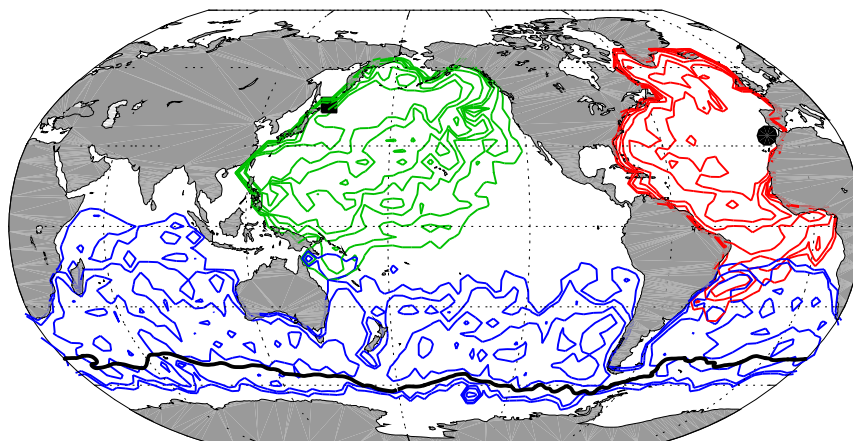


FIG. 14. Normalized density of tracers after 30 years of a constant inflow at (green contours) the Kuril Islands chain (black square), at (red contours) the Strait of Gibraltar (black disk), and at (blue contours) the Polar Front (black line) is imposed in the empirical statistical model. This corresponds to NPIW, MW, and AAIW. Contour lines correspond to 1%, 2%, 5%, 10%, 20%, 50%, and 90% of the global maximum density.

5. Conclusions

Intermediate waters can be characterized by a vertical salinity extremum. In particular, with a vertical equilibrium location around ~ 1000 m, they contribute to the upper limb of the global ocean circulation. Here, to study the evolution of three intermediate waters, we have developed an empirical statistical model based on the transition probability of Argo float displacement during their deep journey.

The asymptotic analysis of this model suggests the existence of 10 principal stationary points that are robust to the impact of observational uncertainty (even if their attractivity can vary by up to 45%). They attract asymptotically more than 97% of the world oceans' tracers. To further determine the importance of these 10 stationary points, we have identified their respective basin of attraction. This suggests the generalization of the concept of attractor in a probabilistic sense, where tracers from a single location can reach several stationary points. In this paradigm, attractors depict the likelihood of tracers to reach each of the 10 principal stationary points.

The asymptotic equilibrium of our statistical empirical model is reached on the order of 1000 yr. Depending on the water masses, the typical convergence time scales are multicentennial or multimillennial. This suggests that water mass properties at ~ 1000 m depth, that is, the typical depth of intermediate waters, takes on the order of 1000 years to fully equilibrate. This result is consistent with numerical model results (Wunsch and Heimbach 2008; Siberlin and Wunsch 2011; Sévellec and Fedorov 2016). This also suggests that numerical models of the ocean and climate need to be run on at least the order of

1000 yr for full adjustment. More fundamentally, this also means that current water masses are the outcome of the past ~ 1000 yr of ocean surface forcing. Given the important uncertainty of the past buoyancy and momentum fluxes to the ocean, mismatch can be expected between current ocean properties and model output.

Using this model, we set experiments to study the evolution of three intermediate waters: the North Pacific Intermediate Water (NPIW), the Mediterranean Water (MW), and the Antarctic Intermediate Water (AAIW). These experiments consist of a constant input (a tracer flux) at the entry point of water masses near 1000 m. Here, we have assumed that intermediate water masses follow constant depth levels rather than isopycnals. This is correct outside outcropping regions (equatorward of 50°S and 50°N), which are mostly outside our studied area. Also, by the use of Lagrangian tracers, we have restricted ourselves to follow an individual material particle of water. This is different from water masses that are transformed through small-scale turbulent processes (which might not be negligible on long millennial time scales). Under these assumptions, we found a striking difference in the asymptotic behavior of the three water masses (Fig. 14). NPIW remains quite local, in the northwestern region of the North Pacific, with intensification in the Kuroshio recirculation; MW spreads regionally inside the North Atlantic subtropical cell; and AAIW fills the ocean globally with its signature in all ocean basins. These results are robust to the observational uncertainty, whereas the choice of the resolution can affect the intensity of the pattern but with only a weak impact on its shape. These results are also consistent with previous analyses of the spread of intermediate water

using a completely independent method (intermediate waters are often tracked as local maximum in salinity; Talley 2008). This both confirms previous analyses and gives credit to our statistical empirical model.

We have shown that our model also provides new insights on the behavior of intermediate waters, such as their probabilistic properties. One other example is the existence of 10 principal stationary points, which are robust to observational error. One hypothesis regarding their existence is that these locations are regions of convergence in the mean horizontal velocity field [following (8)]. However, the probabilistic approach of tracer evolution does not allow us to draw any robust conclusions from mean velocity field. Hence, to answer this question, new tools acknowledging the probabilistic behavior of tracers need to be developed. This will be the goal of future investigations.

Also, when more data will be available, we will be able to increase the resolution, opening the perspective of studying turbulent diffusion. We will also be able to extend this study to other water masses. In particular, Argo float displacements between 1500 and 2000 m will allow us to study the lower limb of the Atlantic meridional overturning circulation (e.g., the fate of Labrador Sea Water).

Acknowledgments. This research was supported by grants from Natural and Environmental Research Council UK (MESO-CLIP, NE/K005928/1 and SMURPHS, NE/N005767/1). F.S. thanks the Université de Bretagne Occidentale for its financial support during his visit in summer 2015.

REFERENCES

- Berloff, P. S., and J. C. McWilliams, 2002: Material transport in oceanic gyres. Part II: Hierarchy of stochastic models. *J. Phys. Oceanogr.*, **32**, 797–830, doi:10.1175/1520-0485(2002)032<0797:MTIOGP>2.0.CO;2.
- , and —, 2003: Material transport in oceanic gyres. Part III: Randomized stochastic models. *J. Phys. Oceanogr.*, **33**, 1416–1445, doi:10.1175/1520-0485(2003)033<1416:MTIOGP>2.0.CO;2.
- , —, and A. Bracco, 2002: Material transport in oceanic gyres. Part I: Phenomenology. *J. Phys. Oceanogr.*, **32**, 764–796, doi:10.1175/1520-0485(2002)032<0764:MTIOGP>2.0.CO;2.
- Bower, A. S., L. Armi, and I. Ambar, 1997: Lagrangian observations of meddy formation during a Mediterranean undercurrent seeding experiment. *J. Phys. Oceanogr.*, **27**, 2545–2575, doi:10.1175/1520-0485(1997)027<2545:LOOMFD>2.0.CO;2.
- , N. Setta, and I. Ambar, 2002: Structure of the Mediterranean Undercurrent and Mediterranean Water spreading around the southwestern Iberian Peninsula. *J. Geophys. Res.*, **107**, 3161, doi:10.1029/2001JC001007.
- Chen, R., J. L. McClean, and S. T. Gille, 2014: Isopycnal eddy diffusivities and critical layers in the Kuroshio Extension from an eddyding ocean model. *J. Phys. Oceanogr.*, **44**, 2191–2211, doi:10.1175/JPO-D-13-0258.1.
- Cimatoribus, A. A., S. S. Drijfhout, M. den Toom, and H. A. Dijkstra, 2012: Sensitivity of the Atlantic meridional overturning circulation to South Atlantic freshwater anomalies. *Climate Dyn.*, **39**, 2291–2306, doi:10.1007/s00382-012-1292-5.
- Colin de Verdière, A., and M. Ollitrault, 2016: Direct determination of the world ocean barotropic circulation. *J. Phys. Oceanogr.*, **46**, 255–273, doi:10.1175/JPO-D-15-0046.1.
- Dellnitz, M., G. Froyland, C. Horenkamp, K. Padberg-Gehle, and A. Sen Gupta, 2009: Seasonal variability of the subpolar gyres in the Southern Ocean: A numerical investigation based on transfer operators. *Nonlinear Processes Geophys.*, **16**, 655–664, doi:10.5194/npg-16-655-2009.
- Freeland, H. J., P. B. Rhines, and T. Rossby, 1975: Statistical observations of trajectories of neutrally buoyant floats in the North Atlantic. *J. Mar. Res.*, **33**, 383–404.
- Froyland, G., K. Padberg, M. H. England, and A. M. Treguier, 2007: Detection of coherent oceanic structures via transfer operators. *Phys. Rev. Lett.*, **98**, 224503, doi:10.1103/PhysRevLett.98.224503.
- , R. M. Stuart, and E. van Sebille, 2014: How well connected is the surface of the global ocean? *Chaos*, **24**, 033126, doi:10.1063/1.4892530.
- Gordon, A. L., 1986: Inter-ocean exchange of thermocline water. *J. Geophys. Res.*, **91**, 5037–5046, doi:10.1029/JC091iC04p05037.
- Hennon, T. D., S. C. Riser, and M. H. Alford, 2014: Observations of internal gravity waves by Argo floats. *J. Phys. Oceanogr.*, **44**, 2370–2386, doi:10.1175/JPO-D-13-0222.1.
- Iorga, M. C., and M. S. Lozier, 1999a: Signatures of Mediterranean outflow from North Atlantic climatology: 1. Salinity and density fields. *J. Geophys. Res.*, **104**, 25 985–26 009, doi:10.1029/1999JC900115.
- , and —, 1999b: Signatures of Mediterranean outflow from North Atlantic climatology: 2. Diagnostic velocity fields. *J. Geophys. Res.*, **104**, 26 011–26 029, doi:10.1029/1999JC900204.
- Jones, D. C., A. J. S. Meijers, E. Shuckburgh, J.-B. Sallée, P. Haynes, E. K. McAufield, and M. R. Mazloff, 2016: How does subantarctic mode water ventilate the Southern Hemisphere subtropics? *J. Geophys. Res.*, **121**, 6558–6582, doi:10.1002/2016JC011680.
- Koszalka, I. M., and J. H. LaCasce, 2010: Lagrangian analysis by clustering. *Ocean Dyn.*, **60**, 957–972, doi:10.1007/s10236-010-0306-2.
- Locarnini, R. A., A. V. Mishonov, J. I. Antonov, T. P. Boyer, H. E. Garcia, O. K. Baranova, M. M. Zweng, and D. R. Johnson, 2010: *Temperature*. Vol. 1, *World Ocean Atlas 2009*, NOAA Atlas NESDIS 68, 184 pp.
- Lucarini, V., 2016: Response operators for Markov processes in a finite state space: Radius of convergence and link to the response theory for Axiom A systems. *J. Stat. Phys.*, **162**, 312–333, doi:10.1007/s10955-015-1409-4.
- Maximenko, N. A., J. Hafner, and P. P. Niiler, 2012: Pathways of marine debris derived from trajectories of Lagrangian drifters. *Mar. Pollut. Bull.*, **65**, 51–62, doi:10.1016/j.marpolbul.2011.04.016.
- Needler, G. T., and R. A. Heath, 1975: Diffusion coefficients calculated from the Mediterranean salinity anomaly in the North Atlantic Ocean. *J. Phys. Oceanogr.*, **5**, 173–182, doi:10.1175/1520-0485(1975)005<0173:DCCFTM>2.0.CO;2.
- Ollitrault, M., and A. Colin de Verdière, 2002: SOFAR floats reveal midlatitudes intermediate North Atlantic General circulation. Part II: An Eulerian statistical view. *J. Phys. Oceanogr.*, **32**, 2034–2053, doi:10.1175/1520-0485(2002)032<2034:SFRMIN>2.0.CO;2.
- , and J. P. Rannou, 2013: ANDRO: An Argo-based deep displacement dataset. *J. Atmos. Oceanic Technol.*, **30**, 759–788, doi:10.1175/JTECH-D-12-00073.1.

- , and A. Colin de Verdière, 2014: The ocean general circulation near 1000-m depth. *J. Phys. Oceanogr.*, **44**, 384–409, doi:[10.1175/JPO-D-13-030.1](https://doi.org/10.1175/JPO-D-13-030.1).
- Orsi, A. H., T. Whitworth, and W. D. Nowlin, 1995: On the meridional extent and fronts of the Antarctic Circumpolar Current. *Deep-Sea Res. I*, **42**, 641–673, doi:[10.1016/0967-0637\(95\)00021-W](https://doi.org/10.1016/0967-0637(95)00021-W).
- Owens, W. B., 1991: A statistical description of the mean circulation and eddy variability in the North western Atlantic using SOFAR floats. *Prog. Oceanogr.*, **28**, 257–303, doi:[10.1016/0079-6611\(91\)90010-J](https://doi.org/10.1016/0079-6611(91)90010-J).
- Richardson, P. L., and K. Mooney, 1975: The Mediterranean outflow—A simple advection–diffusion model. *J. Phys. Oceanogr.*, **5**, 476–482, doi:[10.1175/1520-0485\(1975\)005<0476:TMOSAD>2.0.CO;2](https://doi.org/10.1175/1520-0485(1975)005<0476:TMOSAD>2.0.CO;2).
- Rimaud, J., S. Speich, B. Blanke, and N. Grima, 2012: The exchange of Intermediate Water in the southeast Atlantic: Water mass transformations diagnosed from the Lagrangian analysis of a regional ocean model. *J. Geophys. Res.*, **117**, C08034, doi:[10.1029/2012JC008059](https://doi.org/10.1029/2012JC008059).
- Rossby, H. T., S. C. Riser, and A. J. Mariano, 1983: The western North Atlantic—A Lagrangian viewpoint. *Eddies in Marine Science*, A. R. Robinson, Ed., Springer, 66–91, doi:[10.1007/978-3-642-69003-7_4](https://doi.org/10.1007/978-3-642-69003-7_4).
- Sévellec, F., and A. V. Fedorov, 2014: Millennial variability in an idealized ocean model: Predicting the AMOC regime shifts. *J. Climate*, **27**, 3551–3564, doi:[10.1175/JCLI-D-13-00450.1](https://doi.org/10.1175/JCLI-D-13-00450.1).
- , and —, 2016: AMOC sensitivity to surface buoyancy fluxes: Stronger ocean meridional heat transport with a weaker AMOC? *Climate Dyn.*, **47**, 1497–1513, doi:[10.1007/s00382-015-2915-4](https://doi.org/10.1007/s00382-015-2915-4).
- Shcherbina, A. Y., L. D. Talley, and D. L. Rudnick, 2003: Direct observations of North Pacific ventilation: Brine rejection in the Okhotsk Sea. *Science*, **302**, 1952–1955, doi:[10.1126/science.1088692](https://doi.org/10.1126/science.1088692).
- Siberlin, C., and C. Wunsch, 2011: Oceanic tracer and proxy time scales revisited. *Climate Past*, **7**, 27–39, doi:[10.5194/cp-7-27-2011](https://doi.org/10.5194/cp-7-27-2011).
- Spall, M. A., P. L. Richardson, and J. Price, 1993: Advection and eddy mixing in the Mediterranean salt tongue. *J. Mar. Res.*, **51**, 797–818, doi:[10.1357/0022240933223882](https://doi.org/10.1357/0022240933223882).
- Srokosz, M., M. Baringer, H. Bryden, S. Cunningham, T. Delworth, S. Lozier, J. Marotzke, and R. Sutton, 2012: Past, present, and future changes in the Atlantic meridional overturning circulation. *Bull. Amer. Meteor. Soc.*, **93**, 1663–1676, doi:[10.1175/BAMS-D-11-00151.1](https://doi.org/10.1175/BAMS-D-11-00151.1).
- Stanev, E. V., 1992: Numerical experiment on the spreading of Mediterranean water in the North Atlantic. *Deep-Sea Res.*, **39A**, 1747–1766, doi:[10.1016/0198-0149\(92\)90027-Q](https://doi.org/10.1016/0198-0149(92)90027-Q).
- Stephens, J. C., and D. P. Marshall, 1999: Dynamics of the Mediterranean salinity tongue. *J. Phys. Oceanogr.*, **29**, 1425–1441, doi:[10.1175/1520-0485\(1999\)029<1425:DOTMST>2.0.CO;2](https://doi.org/10.1175/1520-0485(1999)029<1425:DOTMST>2.0.CO;2).
- Suga, T., and L. D. Talley, 1995: Antarctic Intermediate Water circulation in the tropical and subtropical South Atlantic. *J. Geophys. Res.*, **100**, 13 441–13 453, doi:[10.1029/95JC00858](https://doi.org/10.1029/95JC00858).
- Talley, L. D., 1993: Distribution and formation of North Pacific Intermediate Water. *J. Phys. Oceanogr.*, **23**, 517–537, doi:[10.1175/1520-0485\(1993\)023<0517:DAFONP>2.0.CO;2](https://doi.org/10.1175/1520-0485(1993)023<0517:DAFONP>2.0.CO;2).
- , 1996: Antarctic Intermediate Water in the South Atlantic. *The South Atlantic: Present and Past Circulation*, G. Wefer et al., Eds., Springer, 219–238, doi:[10.1007/978-3-642-80353-6_11](https://doi.org/10.1007/978-3-642-80353-6_11).
- , 1997: North Pacific Intermediate Water transports in the mixed water regions. *J. Phys. Oceanogr.*, **27**, 1795–1803, doi:[10.1175/1520-0485\(1997\)027<1795:NPIWTI>2.0.CO;2](https://doi.org/10.1175/1520-0485(1997)027<1795:NPIWTI>2.0.CO;2).
- , 1999: Some aspects of ocean heat transport by the shallow, intermediate and deep overturning circulations. *Mechanisms of Global Climate Change at Millennial Time Scales*, Geophys. Monogr., Vol. 112, Amer. Geophys. Union, 1–22.
- , 2003: Shallow, intermediate, and deep overturning components of the global heat budget. *J. Phys. Oceanogr.*, **33**, 530–560, doi:[10.1175/1520-0485\(2003\)033<0530:SIADOC>2.0.CO;2](https://doi.org/10.1175/1520-0485(2003)033<0530:SIADOC>2.0.CO;2).
- , 2008: Freshwater transport estimates and the global overturning circulation: Shallow, deep and throughflow components. *Prog. Oceanogr.*, **78**, 257–303, doi:[10.1016/j.pocean.2008.05.001](https://doi.org/10.1016/j.pocean.2008.05.001).
- , Y. Nagata, M. Fujimura, T. Iwao, T. Kono, D. Inagake, M. Hirai, and K. Okuda, 1995: North Pacific Intermediate Water in the Kuroshio/Oyashio mixed water region. *J. Phys. Oceanogr.*, **25**, 475–501, doi:[10.1175/1520-0485\(1995\)025<0475:NPIWTI>2.0.CO;2](https://doi.org/10.1175/1520-0485(1995)025<0475:NPIWTI>2.0.CO;2).
- , G. L. Pickard, W. J. Emery, and J. H. Swift, 2011: *Descriptive Physical Oceanography: An Introduction*. 6th ed. Academic Press, 560 pp.
- Tantet, A., F. R. van der Burgt, and H. A. Dijkstra, 2015: An early warning indicator for atmospheric blocking events using transfer operators. *Chaos*, **25**, 036406, doi:[10.1063/1.4908174](https://doi.org/10.1063/1.4908174).
- van Aken, H. M., 2000: The hydrography of the mid-latitude northeast Atlantic Ocean II: The intermediate water masses. *Deep-Sea Res. I*, **47**, 789–824, doi:[10.1016/S0967-0637\(99\)00112-0](https://doi.org/10.1016/S0967-0637(99)00112-0).
- van Sebille, E., L. M. Beal, and W. E. Johns, 2011: Advective time scales of Agulhas leakage to the North Atlantic in surface drifter observations and the 3D OFES model. *J. Phys. Oceanogr.*, **41**, 1026–1034, doi:[10.1175/2011JPO4602.1](https://doi.org/10.1175/2011JPO4602.1).
- , M. H. England, and G. Froyland, 2012: Origin, dynamics and evolution of ocean garbage patches from observed surface drifters. *Environ. Res. Lett.*, **7**, 044040, doi:[10.1088/1748-9326/7/4/044040](https://doi.org/10.1088/1748-9326/7/4/044040).
- , P. Spence, M. R. Mazloff, M. H. England, S. R. Rintoul, and O. A. Saenko, 2013: Abyssal connections of Antarctic Bottom Water in a Southern Ocean state estimate. *Geophys. Res. Lett.*, **40**, 2177–2182, doi:[10.1002/grl.50483](https://doi.org/10.1002/grl.50483).
- Weaver, A. J., E. S. Sarachik, and J. Marotzke, 1991: Freshwater flux forcing of decadal and interdecadal oceanic variability. *Nature*, **353**, 836–838, doi:[10.1038/353836a0](https://doi.org/10.1038/353836a0).
- Wunsch, C., and P. Heimbach, 2008: How long to oceanic tracer and proxy equilibrium? *Quat. Sci. Rev.*, **27**, 637–651, doi:[10.1016/j.quascirev.2008.01.006](https://doi.org/10.1016/j.quascirev.2008.01.006).
- Zika, J. D., T. J. McDougall, and B. M. Sloyan, 2010: A tracer-contour inverse method for estimating ocean circulation and mixing. *J. Phys. Oceanogr.*, **40**, 26–47, doi:[10.1175/2009JPO4208.1](https://doi.org/10.1175/2009JPO4208.1).
- , M. H. England, and W. P. Sijp, 2012: The ocean circulation in thermohaline coordinates. *J. Phys. Oceanogr.*, **42**, 708–724, doi:[10.1175/JPO-D-11-0139.1](https://doi.org/10.1175/JPO-D-11-0139.1).